

Single-laser-based simultaneous four-wavelength excitation source for femtosecond two-photon fluorescence microscopy

YANG-TING HSIAO,¹ YU-FAN HUANG,² BHASKAR JYOTI BORAH,¹ SHIH-KUO CHEN,² AND CHI-KUANG SUN^{1,*} 

¹*Department of Electrical Engineering and Graduate Institute of Photonics and Optoelectronics, National Taiwan University, Taipei 10617, Taiwan*

²*Department of Life Science, National Taiwan University, Taipei 10617, Taiwan*

**sun@ntu.edu.tw*

Abstract: Multicolor labeling of biological samples with large volume is required for omic-level of study such as the construction of nervous system connectome. Among the various imaging method, two photon microscope has multiple advantages over traditional single photon microscope for higher resolution and could image large 3D volumes of tissue samples with superior imaging depth. However, the growing number of fluorophores for labeling underlines the urgent need for an ultrafast laser source with the capability of providing simultaneous plural excitation wavelengths for multiple fluorophores. Here, we propose and demonstrate a single-laser-based four-wavelength excitation source for two-photon fluorescence microscopy. Using a sub-100 fs 1,070-nm Yb: fiber laser to pump an ultrashort nonlinear photonic crystal fiber in the low negative dispersion region, we introduced efficient self-phase modulation and acquired a blue-shifted spectrum dual-peaked at 812 and 960 nm with 28.5% wavelength conversion efficiency. By compressing the blue-shift near-IR spectrum to 33 fs to ensure the temporal overlap of the 812 and 960 nm peaks, the so-called sum frequency effect created the third virtual excitation wavelength effectively at 886 nm. Combined with the 1,070 nm laser source as the fourth excitation wavelength, the all-fiber-format four-wavelength excitation source enabled simultaneous four-color two-photon imaging in Brainbow AAV-labeled (TagBFP, mTFP, EYFP, and mCherry) brain samples. With an increased number of excitation wavelengths and improved excitation efficiency than typical commercial femtosecond lasers, our compact four-wavelength excitation approach can provide a versatile, efficient, and easily accessible solution for multiple-color two-photon fluorescence imaging in the field of neuroscience, biomolecular probing, and clinical applications with at least four spectrally-distinct fluorophores.

© 2021 Optical Society of America under the terms of the [OSA Open Access Publishing Agreement](#)

1. Introduction

The brain exhibits one of the most complex morphology owing to the intricate intraneuronal interactions between billions of neurons. Investigation in such a complex system has been relied upon multicolor fluorescence imaging and various biomarkers, providing distinct spectral information according to cell features. Moreover, simultaneous multicolor labeling with more than three colors has been increasingly used to gain more comprehensive insights in brain studies. For example, Brainbow is a multicolor labeling technique based on three or four fluorescent proteins (FPs) for mapping neuronal connectivity by creating hundreds of hues to achieve single-cell labeling [1–3]. In addition, multi-color imaging were also used for various application such as four-color imaging for functional imaging with genetically encoded calcium indicators [4], six-color labeling for characterizing cellular interaction [5], and ten-color immunostaining for an alternative approach to study neural network [6].

The increasing number of fluorescent tags for labeling has led to challenges for imaging systems, particularly for two-photon microscopy that requires expensive and bulky solid-state lasers with laborious maintenance. To implement two-photon fluorescence microscopy (TPFM), which mitigates serious background noise and the risk of out-of-focus photobleaching in single-photon microscopy [7–10], a wavelength-tunable Ti:sapphire (Ti:S) femtosecond oscillator has often been used to excite multiple fluorescent tags sequentially [11]. However, during wavelength tuning and repetitive scanning, the long scanning duration may lead to sample instability [12,13]; sequential excitation is also incompatible for fast event functional studies [14]. Therefore, there is an urgent need to develop a source that can simultaneously provide multiple excitation wavelengths for TPFM.

Nevertheless, unlike the rapid progression of multicolor labeling, the existing simultaneous multicolor excitation source can only provide three excitation wavelengths by means of either nonlinear optics [15] or fiber technologies [16,17]. For example, Mahou et al. earlier attempted to introduce sum-frequency generation (SFG) from a Ti:S laser and a synchronized optical parametric oscillator (OPO) with an additional delay control to create the third virtual excitation wavelength [15]. This system has contributed to three-XFP based Brainbow imaging; it had also been adopted for simultaneous five-color and six-color fluorescence imaging [18]. However, this multi-laser-based excitation system has limited capacity to efficiently excite all the five or six fluorophores; the system also compromised on using two red FPs (tdTomato and mCherry) with spectrally-close two-photon absorption (TPA) spectra to achieve four-color imaging.

To address the issue of size and cost of the multi-laser-based system, Wang et al. had generated three wavelengths at 775, 864, and 950 nm by using nonlinear crystals to double the frequencies of an energetic Er:fiber laser and red-shift frequencies from a large-mode-area photonic crystal fiber (PCF) [16]. Another approach with improved system simplicity used a highly nonlinear PCF (HNPCF) to generate 750, 1,030, and 1,230 nm by Cherenkov radiation (CR) and soliton self-frequency shift (SSFS) [17]. These inspiring approaches with simultaneous three excitation wavelengths, however, exhibit limited performance when adopting more than three fluorescent tags with spectrally distinct TPA spectra. For example, the adeno-associated virus based four-XFP Brainbow (Brainbow AAV), which has the broadest TPA range among the Brainbow series and wide applicability to various tissues and species [2], remains unavailable in TPFM due to its spectrally distinct TPA peaks approximately located at 810 [19,20], 870 [19,20], 970 [19,20], and 1,080 nm [19,20] for blue, cyan, yellow, and red FPs, respectively. Therefore, a four-wavelength excitation source is required to obtain the highest amount of color information. As a result, it poses a great challenge to femtosecond light source development with a minimum of four excitation wavelengths for simultaneous greater-than-or-equal-to four-color imaging in TPFM.

In this paper, we report the development of a femtosecond four-wavelength excitation source for TPFM. Using a 1,070-nm Yb:fiber femtosecond laser to pump a HNPCF with a length shorter than the soliton fission length, self-phase modulation (SPM) [21] in the weak negative dispersion region created a blue-shifted spectrum dual-peaked at 812 and 960 nm. By compressing the blue-shift near-IR spectrum to 33 fs to ensure the temporal overlap of the 812 and 960 nm peaks, the SFG effect created the third virtual excitation wavelength [15] at 886 nm. Combined with the 1,070 nm pumping source, the four-wavelength excitation source enabled simultaneous four-color imaging of Brainbow AAV-labeled *ex-vivo* brain samples expressing four spectrally distinct FPs: blue TagBFP, cyan mTFP, yellow EYFP, and red mCherry. Our demonstration combining the merit of additional virtual SFG wavelength effect and compactness of fiber-enabled SPM serves as a firstly proposed strategy, to the best of our knowledge, for designing a multi-spectral excitation source based on one laser. The simple and efficient fiber-format approach with simultaneous four excitation wavelengths would also support the wide applicability of the TPFM imaging not just of four-XFP based Brainbow AAV but also other multicolor visible fluorescent tags.

2. Materials and methods

2.1. Experimental setup of the four-wavelength excitation source, two-photon excitation spectroscopy and two-photon fluorescence microscopy

Figure 1 depicts the four-wavelength excitation source. The pumping source for SPM-enabled blue-shifting was a Yb:fiber laser (Fidelity-2, Coherent) emitting 48 fs pulses (assuming a Gaussian shape) centered at 1,070 nm with a 70 MHz repetition rate. SPM-enabled wavelength conversion was implemented by coupling the femtosecond pulses into a 6.5 mm HNPCF (SC-5.0-1040, NKT Photonics) with a zero-dispersion wavelength of 1,040 nm using an aspheric lens (A375TM-C, Thorlabs) and a manual three-axis stage (MAX350D, Thorlabs). Both end facets of the HNPCF were collapsed to mitigate laser-induced degradation. Wavelength conversion was then optimized by power regulation provided by a half-wave plate and a polarizing beam splitter. A customized bandpass filter (BPF) was applied to select a wavelength range of 750–1,000 nm from the HNPCF-output. The filtered HNPCF-output pulse and the 1,070 nm pulse were respectively pre-chirped by a grating pair compressor (Fig. 1(b)) and a prism pair compressor (Fig. 1(c)) before being combined by a short-pass dichroic mirror. The HNPCF-output pulse will be compressed and serve as a three-wavelength (TW) excitation pulse, including 812, 886, and 960 nm, for further studies on excitation performance, and will be combined with the 1,070 nm pulse for the demonstration of simultaneous four-color excitation in TPFM. The laser spectrum and the pulse width were measured by a laser spectrometer (WaveScan, APE GmbH) with a 500–1,600 nm detection range and an intensity autocorrelator (AC-100ps, UVisIR), respectively.

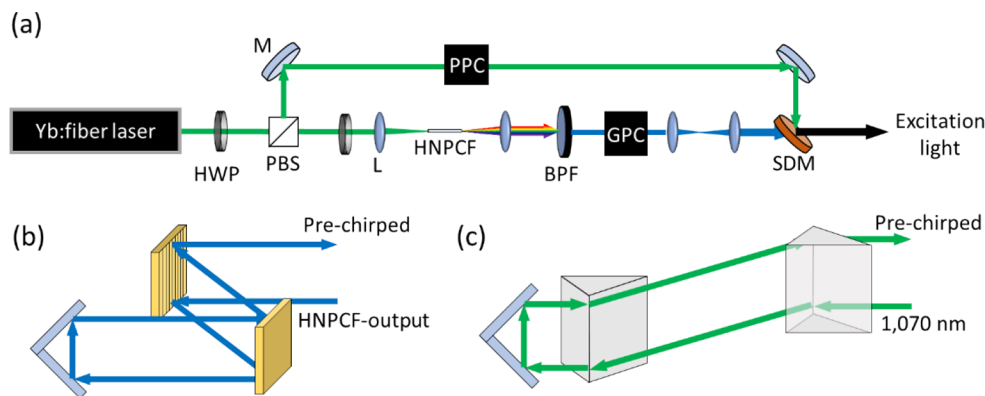


Fig. 1. (a) System schematic of the four-wavelength excitation source. HWP: half-wave plate; PBS: polarizing beam splitter; L: lens; BPF: band-pass filter; PPC: prism pair compressor; GPC: grating pair compressor; SDM: short-pass dichroic mirror. (b) Configurations of GPC. Diffraction gratings are manufactured with 300 lines/mm and an 8.6° blaze angle. (c) Configurations of PPC. The prisms are made of SF10 glass and cut with a Brewster angle of 59.7° and an apex angle of 60.6° .

For studies on excitation performance, including excitation efficiency, virtual wavelength generation, and Brainbow AAV fluorescence measurement, we used a compact fluorescence spectrometer (EagleEye, OtO Photonics) with a 0°C internal cooling charge-coupled device (CCD) as shown in Fig. 2. Fluorescence was collected by a long-pass dichroic mirror (LDM) with a cut-on wavelength at 655 nm (FF655-Di01, Semrock) and reflected to the fiber collection head of the spectrometer. A BPF (FESH0700, Thorlabs) was also added to mitigate the excitation leakage from the fiber-supercontinuum.

For excitation efficiency comparison, we compared the single-TW-pulse-excited fluorescence intensity and that excited by a commercial Ti:S laser (Chameleon Ultra II, Coherent). Note that

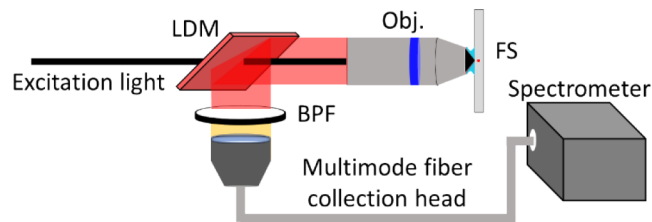


Fig. 2. System schematic of two-photon spectroscopy. LDM: long-pass dichroic mirror with a cut-on wavelength at 655 nm; BPF: a band-pass filter enabling 400–700 nm; Obj.: the 40× or 50× objective lens; FS: fluorescent solution.

for the use of Brainbow AAV in spectroscopy, serious signal degradation occurs when exciting a fixed sample position and the color expression is position-dependent, making a fair comparison impossible. Thus, we used commercially available fluorescent solutions that, to the best of our knowledge, had the closest TPA peaks to those of TagBFP, mTFP, and EYFP, with uniform concentration. Rhodamine 110 (Rh110) and Alexa Fluor 488 (AF488), which have TPA peaks at 800 and 950 nm, respectively [22], along with Lucifer yellow (LY), which has two local peaks at 840 and 880 nm [23], were used to study the excitation efficiency of our TW pulse. The Ti:S laser was tuned to 810, 870, and 970 nm to excite Rh110, LY, and AF488, respectively, simulating three excitation conditions for TagBFP, mTFP, and EYFP. When exciting Rh110 and LY, we applied a 40× objective lens (UApo/340, Olympus, NA = 0.90) for both the TW pulse and the Ti:S laser pulse, whereas a 50× one (LCPlanFLN, Olympus, NA = 0.70) was applied for exciting AF488 because of its higher transmission at 970 nm.

For the spectroscopy study on the virtual wavelength effect, we followed the similar approach of Ref. [15], which compared the fluorescence intensity excited by the sum frequency of two synchronized pulses at different time delays. We stretched the TW pulse using the grating pair compressor when exciting Rh110, LY, and AF488 in the configuration in Fig. 2 with the 40× objective lens for experimental validation. For further numerical validation, we calculated spectrograms at two crucial grating-induced pulse-stretching conditions, denoted as optimal virtual wavelength (OVW) condition and negligible virtual wavelength (NVW) condition. The OVW and NVW conditions are defined as ≈ 0 fs time delay and > 500 fs time delay between the 812 and 960 nm peaks, respectively. For the spectroscopy study, the OVW condition corresponds to the shortest compressed pulse width, which is 26 fs, after the 40× objective. By assuming that the shortest pulse was acquired by compensating the group delay dispersion (GDD) to roughly zero, we set the OVW dispersion to $\text{GDD} = 0 \text{ fs}^2$ and third order dispersion (TOD) = $1,340 \text{ fs}^3$, with 20 fs^2 and 100 fs^3 uncertainties. The additional grating-induced dispersion of the NVW condition can then be calculated based on the extra displacement and will be represented by the change in GDD (ΔGDD) and TOD (ΔTOD). Spectrograms were calculated based on the absolute values of the OVW condition and the additional modification on GDD and TOD due to the grating pair displacement from the OVW condition.

For Brainbow AAV fluorescence measurement, we adopted the same configuration as in Fig. 2 but with another imaging spectrometer (SR303i, Andor) with a cooled CCD at -75°C . Fluorescence was collected and collimated by the 40× objective lens and focused by an achromatic doublet (DLB-150-PM, SIGMAKOKI), instead of the fiber collection head, into the spectrometer entrance slit.

TPFM is conducted using our home-built two-photon microscope [24] as shown in Fig. 3(a). The four-wavelength excitation light excited samples through a 20× water-immersion objective lens (XLUMPlanFI, Olympus, NA = 0.95), which is also used for collecting fluorescence. The

collected fluorescence was reflected by an LDM with a cut-on wavelength at 735 nm (FF735-Di01-50 × 50, Semrock) and separated to four different detection channels by using a series of LDMs with cut-on wavelengths at 560 (FF560-Di01-50 × 50, Semrock), 505 (T505-lpxr, Chroma), and 473 nm (Di03-R473-t1-50 × 50, Semrock). In front of the photo-multiplier tube (PMT) in each detection channel, we used several spectral filters (FF01-618/50-25, FF01-525/50-25, Semrock; FESH0700, FGB37-A, Thorlabs) to design the detection wavelength ranges at 437/94, 494/18, 529/48, and 618/56 nm, representing blue, cyan, yellow, and red channels, respectively, as shown in Fig. 3(b). Two-photon imaging was conducted at room temperature (19°C) without cooling systems for PMTs. For demonstrating simultaneous four-XFP based Brainbow AAV imaging in TPFM, we used the four-wavelength pulses, which consisted of the compressed TW pulse of 33 fs and the 1,070 nm pulse, as a multi-spectral excitation light for the four spectrally distinct FPs. No fluorescence signal was observed outside the labeled area. The theoretical lateral resolutions for 812, 886, 960, and 1,070 nm obtained using the 20× objective lens were 325, 355, 385, and 429 nm, respectively [25]. The experimental lateral resolutions in the blue, cyan, yellow, and red channels measured from the observable structure of the four-XFP-labeled sample were 374, 517, 565, and 588 nm, respectively.

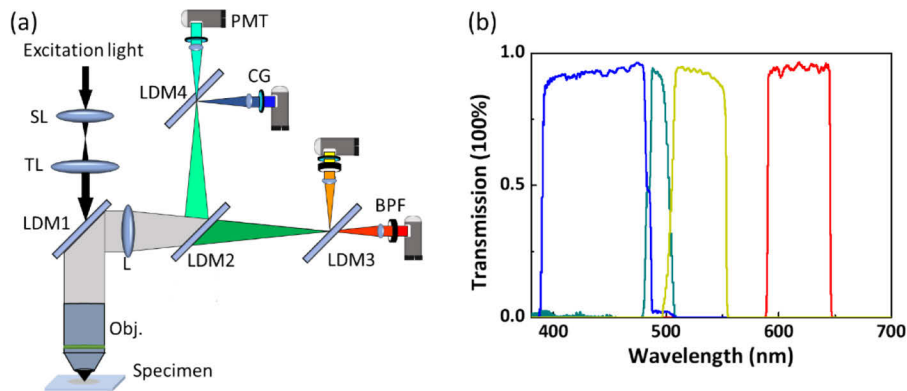


Fig. 3. (a) Schematic of the excitation and detection system in the two-photon microscope. SL: scan lens; TL: tube lens; L: lens; LDM: long-pass dichroic mirror; LDM1: cut-on 735 nm; LDM2: cut-on 505 nm; LDM3: cut-on 560 nm; LDM4: cut-on 473 nm. Obj: the 20× objective lens; PMT: photo-multiplier tube; CG: colored-glass filter. BPF: band-pass filter (b) Calculated spectral transmissions of the four-channel detection system. Each spectral transmission can be represented with a central wavelength and a full width at half maximum bandwidth. Blue curve: 437/94 nm; cyan curve: 494/18 nm; yellow curve: 529/48 nm; red curve: 618/56 nm.

For the microscopy study on the virtual wavelength effect, by again following the similar approach of Ref. [15], we compared the image intensity of TagBFP, mTFP, and EYFP at OVW and NVW conditions. We first adjusted the grating pair compressor to acquire the shortest 33-fs TW pulse after the 20× objective lens, corresponding to the OVW condition, and then adjusted the gratings to introduce ΔGDD and ΔTOD . Spectrograms were calculated in order to duplicate the similar NVW condition as in the virtual wavelength spectroscopy study.

2.2. SPM-enabled wavelength conversion in a 6.5 mm-long HNPCF

Before determining the final excitation spectrum for TagBFP, mTFP, and EYFP, we took advantage of the power-scaling feature of the SPM-dominated spectral broadening to optimize the energy of the converted wavelength [26]. Starting from coupling at an 843 mW average power into a 10-mm-long HNPCF, we shifted the peak wavelength close to 810 nm, which is the TPA peak

of TagBFP, to compensate for the low two-photon brightness of TagBFP [19,20], as shown in Fig. 4(a). Since the power of the converted wavelength could be enhanced by shortening the fiber [26], we further shortened the HNPCF to 8 mm to enable 1,081 mW pumping. As shown in Fig. 4(c), a spectral power close to 810 nm was experimentally optimized by cleaving the HNPCF to 6.5 mm to allow 1,179 mW pumping power while maintaining the spectrum shape. The red dashed boxes in Fig. 4 show the spectral range to be filtered by the customized BPF, with the filtered powers corresponding to the 10, 8, and 6.5 mm HNPCF being 212, 260, and 336 mW, respectively. The average coupled 1,070 nm power of 1,179 mW (16.8 nJ) corresponded to a coupling efficiency of approximately 65%. With the combination of the nonlinear phase change and the high nonlinearity constant [27], another peak at 960 nm, which was close to the 970 nm TPA peak wavelength of EYFP, was simultaneously generated together with the shifted spectral peak at 812 nm, forming a dual-spectral-peaked pulse at the HNPCF-output. The filtered fiber-output pulse with dual peaks at 812 and 960 nm had a 336-mW average power (4.6-nJ), corresponding to a 28.5% blue-shift wavelength conversion efficiency. Through pulse compression, we expect to achieve the SFG effect at the central wavelength of 886 nm, for the excitation of mTFP via virtual excitation wavelength enhancement by temporal overlapping of the 812 and the 960 nm within the same optical pulse. The compressed pulse after the objective served as the TW pulse with three two-photon excitation wavelengths of 812, 886, and 960 nm.

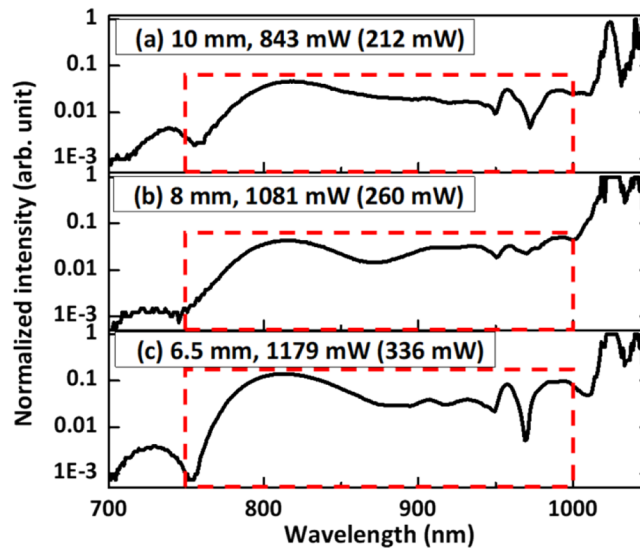


Fig. 4. Output spectra of (a) 10 mm HNPCF coupled with 843 mW, (b) 8 mm HNPCF coupled with 1,081 mW, and (c) 6.5 mm HNPCF coupled with 1,179 mW. The filtered spectral powers shown in the red dashed boxes acquired from the 10, 8, and 6.5 mm HNPCF were 212, 260, and 336 mW, respectively.

In Figs. 5(a)–(d), the excitation pulse spectra and their autocorrelation traces without passing through neither the two-photon microscope nor the compressor are shown. Due to the strong material dispersion in the two-photon microscope system (Fig. 3(a)), further pulse compression was performed by adjusting the distance between prisms or gratings while monitoring the intensity autocorrelation of the light collimated by using another singlet aspheric lens (C230TMD-C, Thorlabs) placed after the 20 \times objective lens. The shortest measured autocorrelation traces are shown in Figs. 5(e) and (f), exhibiting 73 and 33 fs pulse widths for the 1,070 nm and the TW pulses, respectively. The material dispersions of the collimating singlet can be calculated as 354 and 278 fs² at 886 and 1,070 nm, respectively. Hence, before conducting two-photon imaging

or fluorescence measurement, the pulse compressors were slightly adjusted until the brightest possible fluorescence was acquired to compensate for the collimating lens introduced dispersion.

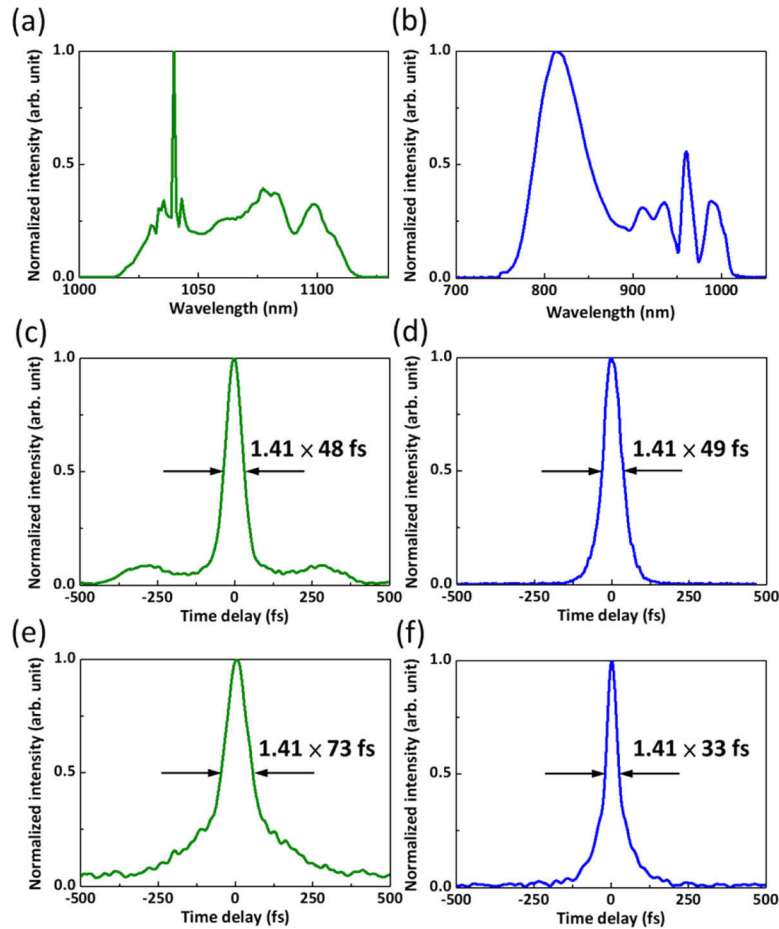


Fig. 5. Spectra of the (a) Yb:fiber laser and (b) filtered output after the 6.5 mm-long HNPCF. (c) and (d) show the corresponding intensity autocorrelation traces of (a) and (b) without neither compression nor passing through the microscope system. Compressed autocorrelation traces measured after the 20 \times objective lens of the microscope are shown in (e) and (f) respectively. The autocorrelation trace widths are labeled with a deconvolution factor and a derived pulse width. The deconvolution factor of 1.41 was applied by the assumption of a Gaussian function.

2.3. Adeno-associated virus-mediated Brainbow processed mouse brain

For demonstrating simultaneous four-color imaging, the cortex of wild-type mice (8–12 weeks old) were co-injected with 0.3 μ L of mixed viral vectors, containing 2.6×10^{12} genome copies per milliliter (mL) of AAV-Brainbow mTFP/mCherry (45186-AAV9, Addgene), 2.6×10^{12} genome copies per mL of AAV-Brainbow TagBFP/EYFP (45185-AAV9, Addgene), and 6.0×10^{11} genome copies per mL of AAV-CAG-Cre recombinase (13775, Addgene). Injection coordinate of the cortex was 0.7 mm posterior to the bregma, 1.0 mm lateral to the midline, and 1.2 mm ventral to the skull surface. For the virtual wavelength study and for color calibration, 1.0 μ L of AAV-Brainbow mTFP/mCherry (1.3×10^{13} genome copies per mL) was injected into the right

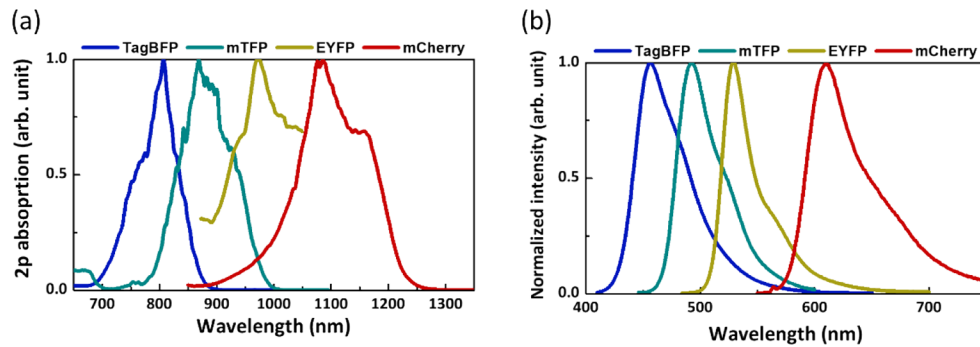


Fig. 6. (a) Two-photon absorption spectra and (b) two-photon emission spectra of AAV-Brainbow. Spectrum data were acquired from an online-available database and re-plotted [20].

side of the cortex of vGAT-Cre mice (36–40 weeks old), whereas AAV-Brainbow TagBFP/EYFP was injected into the left side at the same volume and titer. Injection coordinate of the cortex at each side was 1.3 mm posterior, 3.0 mm lateral, and 0.5 mm ventral to the bregma. Mice were perfused with 50 mL of 4% paraformaldehyde (PFA) 1 month after the injection. Brains were dissected after perfusion and incubated in 4% PFA overnight in 4°C. Brains were coronally sectioned at 80 μm using vibrotome (Campden Instruments, UK) and mounted in rapid clear (SunJin Lab) before observation.

3. Results

3.1. Study on the two-photon excitation efficiency

We compared the single-TW-pulse-excited fluorescence intensity and that excited by a commercial Ti:S laser (Chameleon Ultra II, Coherent). Figures 7(a)–(c) show the measured spectra excited by the two different femtosecond sources with the same pulse energy. For Ti:S excitation, Rh110 was excited by a 0.33 nJ, 110 fs pulse at 810 nm; LY was excited by a 0.23 nJ, 129 fs pulse at 870 nm; and AF488 was excited by a 0.30 nJ, 102 fs pulse at 970 nm. The same TW pulse was therefore adjusted to the equivalent pulse energy for exciting each fluorescent solution accordingly. The measured spectra of the fluorescent solutions shown in Figs. 7(a)–(c) reveal that the fluorescence excited by the compressed TW pulse with dual-spectral-peaks of 812 and 960 nm was stronger than that excited by the commonly adopted femtosecond Ti:S laser source. With the same single-pulse energy, our TW pulse exhibited 2.0, 3.3, and 1.4 times higher excitation efficiency than the commercial Ti:S source at 810, 870, and 970 nm, respectively. This also indicates that simultaneous three-excitation wavelength, high excitation efficiency, and lower pulse energy (since only one pulse will be needed instead of three) can be achieved all at the same time. Additionally, besides the spectral peaks of 812 and 960 nm, the particularly higher excitation efficiency near 870 nm (Fig. 7(b)) can be attributed to the 812 and 960 nm SFG-enabled virtual wavelength effect after pulse compression.

3.2. Study on the virtual wavelength effect

To validate the virtual wavelength excitation effect observed in Fig. 7(b), we compared the fluorescence intensities of Rh110, LY, and AF488 at different pulse-stretching conditions, as shown in Fig. 8(a). With an extra grating displacement of 7.5 mm or greater than the case of the fully compressed pulse, the ΔGDD and ΔTOD will be equivalent to or greater than 1697 fs^2 and 2470 fs^3 respectively and thus the temporal delay between the 812 and 960 nm spectral components will be equivalent to or greater than 580 fs, based on the spectrogram

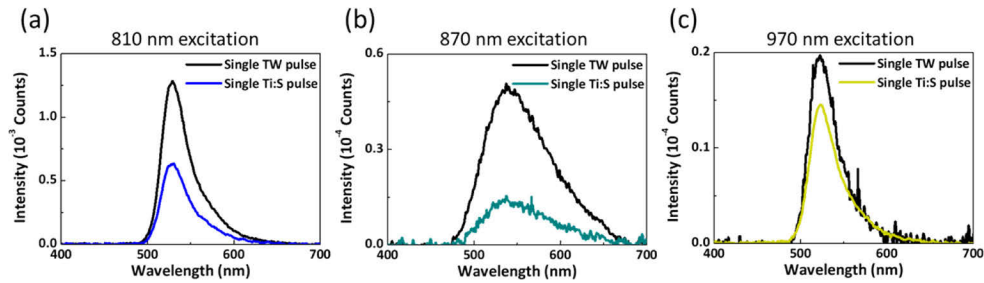


Fig. 7. Two-photon single-pulse-excited fluorescence spectra of (a) Rh110 excited by the compressed TW pulse (black line) and a 110 fs pulse (blue line) at 810 nm, both with 0.33 nJ; (b) LY excited by the compressed TW pulse (black line) and a 129 fs pulse (cyan line) at 870 nm, both with 0.23 nJ; and (c) AF488 excited by the compressed TW pulse (black line) and a 102 fs pulse (yellow line) at 970 nm, both with 0.30 nJ. The lower signal-to-noise ratio of the black curve in (c) was caused by the visible light leakage from the fiber-supercontinuum.

calculation as shown in Fig. 8(c). Without the temporal overlap of the 812 and 960 nm spectral components, called the NVW condition, we expected no SFG virtual wavelength effect and thus the fluorescence intensities of Rh110, LY, and AF488 decreased following the same trend as we lengthened our broadband pulse (Fig. 8(a)). As we compressed the pulse toward the OVW condition with only a 26-fs pulse width, 1.2–1.7 times relative fluorescence intensity enhancement of Rh110 and AF488 can be observed, due to the compressed temporal photon density of the 812 and 960 nm spectral components, while the 2.9 times fluorescence intensity enhancement of the LY cannot be simply explained only by the compressed temporal photon density. We attributed the excess fluorescence intensity enhancement of the LY at the OVW condition to the SFG virtual wavelength effect (at 886 nm) with the full temporal overlap of the 812 and 960 nm spectral components.

Following our spectroscopic studies, we further validated the observation of SFG virtual wavelength effect in mTFP excitation under TPFM imaging. In this microscopy study, the TW pulse with 30 mW (0.43 nJ) was used to excite brain slices either expressing TagBFP and EYFP, or expressing mTFP and mCherry with single Brainbow AAV injection. We acquired images under two different pulse conditions but at a fixed imaging position and with a fixed PMT bias. The OVW condition corresponds to the shortest 33 fs pulse width after compression with roughly 0 fs time delay between the 812 and 960 nm peaks. Compared to the OVW condition, we also displaced the grating pairs with 7.5 mm, corresponding to approximately 580 fs temporal delay between the two peaks following the spectrogram calculation, thus satisfying the NVW condition. Pulses compressed and with an extra grating displacement were applied to TPFM imaging of the TagBFP/EYFP-expressing brain region, and the mTFP/mCherry-expressing brain region, for the fluorescence intensity comparison between TagBFP, EYFP, and mTFP. In Figs. 9 (a)–(f), we show the acquired TPFM images from the corresponding PMT channels of TagBFP, EYFP, mTFP under the OVW and NVW conditions. Images of the three FPs were denoised with the same process, using a mean filter only in Fiji [28], while no frame average was applied. Through a simple fluorescence intensity integration over the whole images, one can find that with the compressed pulse, the TagBFP, EYFP were both enhanced 1.3–1.1 times compared to the specific NVW condition, while a strong enhancement of 2.8 times can be found for mTFP, similar to the spectroscopy study shown in Fig. 8. The excessive enhancement under the OVW condition once again confirmed the contribution from the SFG virtual wavelength effect, at 886 nm, when the 812 and 960 nm spectral components were overlapped temporally.

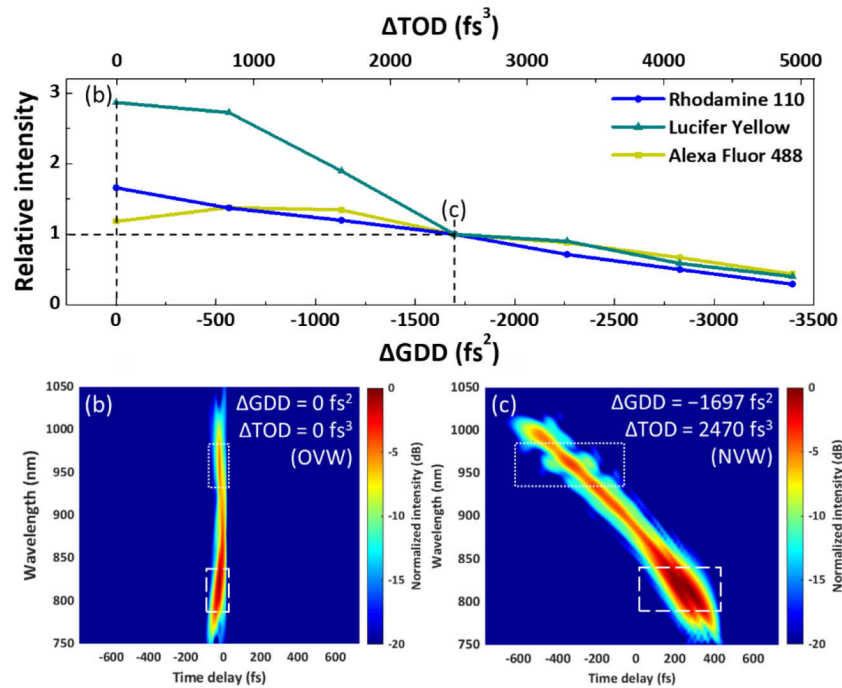


Fig. 8. (a) Relative fluorescence intensities (normalized to that at the NVW condition) of RH110, LY, and AF488 excited by the TW pulse with different relative GDD (ΔGDD) and TOD (ΔTOD) values. Corresponding spectrograms of the excitation pulses are shown in (b) for the OVW condition and in (c) for one specific NVW condition represented in (a). The white dashed boxes and white dotted boxes represent the temporal distributions of the 812/50 and 960/50 nm components, respectively.

3.3. Simultaneous adeno-associated virus based four-XFP Brainbow AAV imaging

The above virtual wavelength study confirmed the tri-excitation wavelengths of 812, 960, and 886 nm of the compressed TW pulse for the two-photon excitation of TagBFP, EYFP and mTFP. Combining the 1,070 nm pulse for the two-photon excitation of mCherry, the four-excitation-wavelength source can therefore be used to demonstrate simultaneous four-XFP based Brainbow AAV TPFM imaging.

The 1,070 nm pulse was first applied for the two-photon excitation of the mTFP/mCherry-expressing brain region. As shown in Fig. 10(a), our spectroscopy measurement indicated that when enabling the 1,070 nm pulse alone, only mCherry was found fluorescing. In contrast, when enabling the compressed TW pulse alone, not only mTFP was successfully excited, a weak mCherry emission can also be found, as shown in Fig. 10(b). With the capability to efficiently excite the TagBFP and EYFP, we also used the same TW pulse alone to excite the four-XFP-labeled Brainbow AAV sample, with the expected additional appearance of the TagBFP and EYFP fluorescence peaks as shown in Fig. 10(c). The weak TagBFP fluorescence was attributed to its ultra-low two-photon brightness. Finally, in Fig. 10(d), with the further addition of the 1,070 nm pulse to provide efficient two-photon excitation of mCherry, the capability of simultaneous two-photon four-color excitation with our four-wavelength source was spectrally validated.

In our demonstration of multi-color TPFM of the Brainbow AAV samples, the 30 mW (0.43 nJ) 33-fs TW pulse and the 20 mW (0.29 nJ) 73 fs 1,070 nm pulse, with respectively $73 \mu W/\mu m^2$ and $49 \mu W/\mu m^2$ excitation intensities applicable for in vivo studies [4,29–32], were first applied

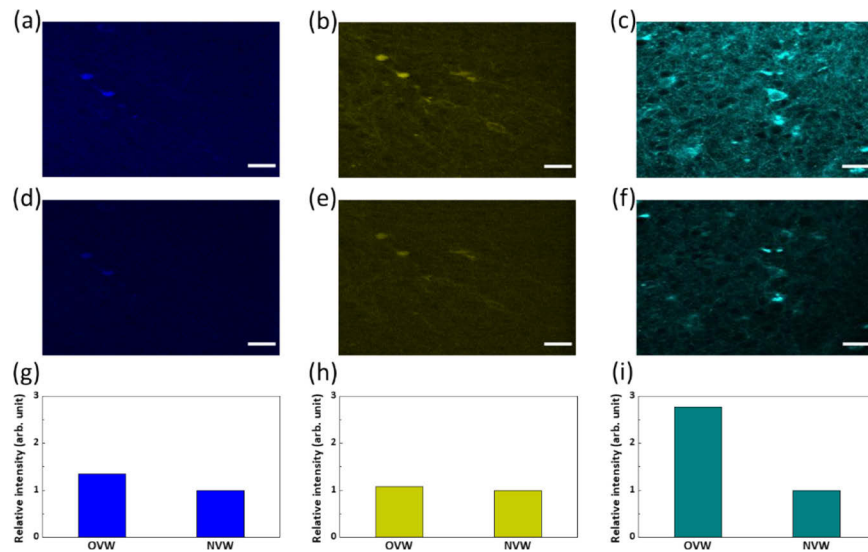


Fig. 9. TPFM images acquired in the TagBFP/EYFP-expressing brain region and the mTFP/mCherry-expressing brain region with the TW pulse excitation under (a–c) the OVW condition and (d–f) the NVW condition. (g–i) Image intensities integrated from the whole image ($3,814 \times 4,096$ pixels) and normalized to that at the NVW condition. (a), (d), (g) correspond to the TagBFP blue channel. (b), (e), (h) correspond to the EYFP yellow channel. (c), (f), (i) correspond to the mTFP cyan channel. Images shown were cropped to $3,462 \times 2,262$ pixels from the whole images. Image pixel intensities were all enhanced by two times for the sake of clarity. Scale bar: $50 \mu\text{m}$.

for the study of the cross-excitation and cross-talk effects and for the color calibration process in different imaging channels. In Fig. 11, we show images of the mTFP/mCherry-expressing brain region, excited either by the $1,070 \text{ nm}$ pulse (Fig. 11(a)) or the compressed TW pulses (Fig. 11(b)), and the TagBFP/EYFP-expressing brain region excited by the compressed TW pulses (Fig. 11(c)). It is noted that in Fig. 11(b), the weak mCherry fluorescence (following Fig. 10(b)) became almost invisible in the red channel, whereas the mTFP glowed strongly with serious spectral bleed-through into the yellow and blue channels, of which the relative magnitudes were afterward used for color linear unmixing [33,34]. For the other two cases, the fluorescence leakage and cross-excitation were both negligible under our system setting. Please note that the PMT voltage in the blue channel was adjusted higher because of the weaker fluorescence.

Finally, the 33-fs TW pulse and the 73 fs $1,070 \text{ nm}$ pulse were combined and sent to the four-XFP-labeled, $80\text{-}\mu\text{m}$ -thick mice brain slice expressing TagBFP, mTFP, EYFP, and mCherry to enable combinatorial expression. Figures 12(a)–(f) and (g)–(l) respectively show images with individual- and merged-color expressions at the same location but acquired at two different depths, 20 and $34 \mu\text{m}$, of the mice brain slice. Minimum frame average (2 frames) was applied for image quality. Images showing mCherry (Figs. 12(a) and (g)), EYFP (Figs. 12(b) and (h)), mTFP (Figs. 12(c) and (i)), and TagBFP (Figs. 12(d) and (j)) fluorescence contrasts were merged to generate the four-XFP Brainbow AAV images (Figs. 12(e) and (k)) acquired through our simultaneous excitation scheme. Linear unmixing was applied. Overall, our results confirmed the feasibility of efficient simultaneous four-color imaging in TPFM using our single-laser-based, fiber-format, four-wavelength excitation source.

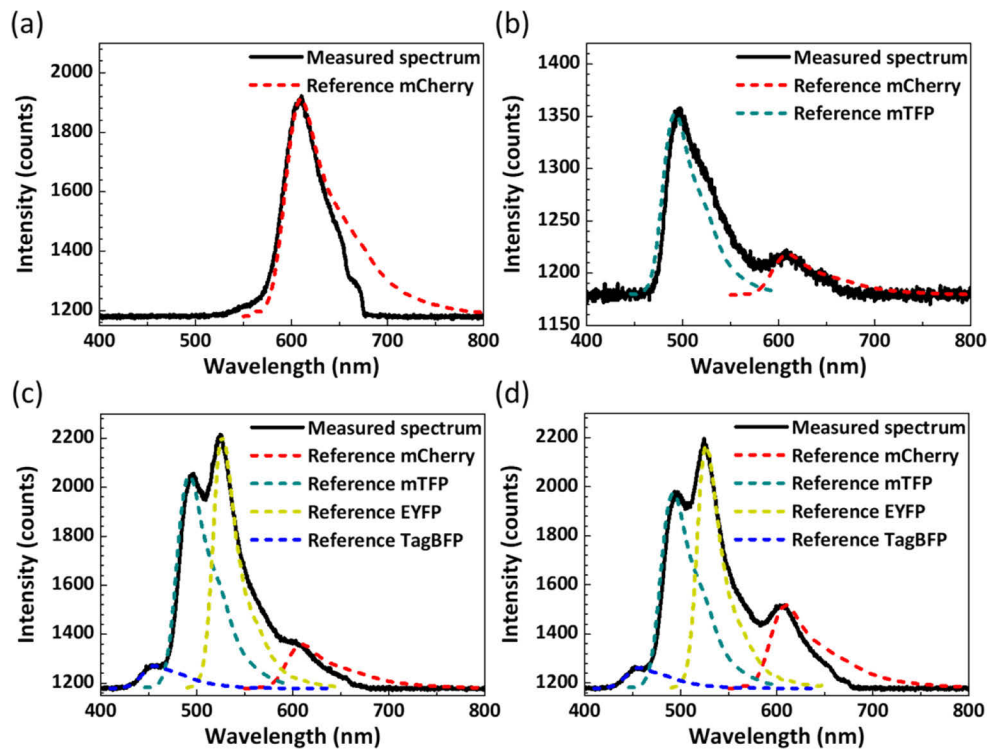


Fig. 10. Measured fluorescence spectra (black solid lines) from (a, b) the mTFP/mCherry-expressing brain region and (c, d) the four-XFP-labeled brain slice. (a) was excited by the 1,070 nm pulse. (b) and (c) were excited by the compressed TW pulse. (d) was excited by the combined 1,070 nm pulse and the compressed TW pulse. The dashed lines with different colors show the reference emission spectra of each FP: red (mCherry), yellow (EYFP), cyan (mTFP), and blue (TagBFP).

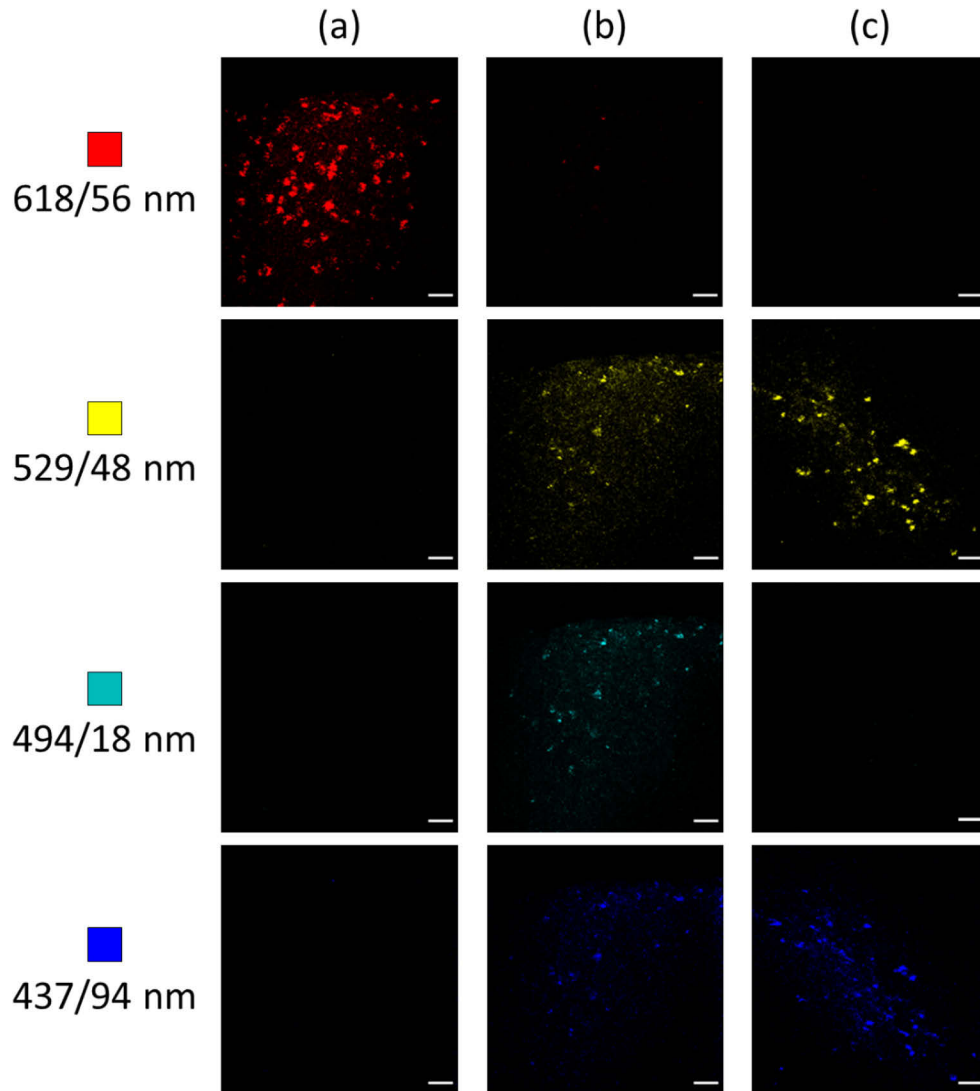


Fig. 11. Two-photon fluorescence images of (a) the mTFP/mCherry-expressing brain region excited by the 1,070 nm pulse, (b) the mTFP/mCherry-expressing brain region excited by the 33-fs TW pulse, and (c) the TagBFP/EYFP-expressing brain region excited by the 33-fs TW pulse. The detected fluorescence images from each individual channel, red (618/56 nm), yellow (529/48 nm), cyan (494/18 nm), and blue (437/94 nm), were shown from top to bottom. The pixels intensities of all images were enhanced by three times for the sake of clarity. The left side of the figure shows the corresponding detected wavelength and adopted pseudo color. Image size: $1,937 \times 2,048$ pixels. Scale bar: 50 μm .

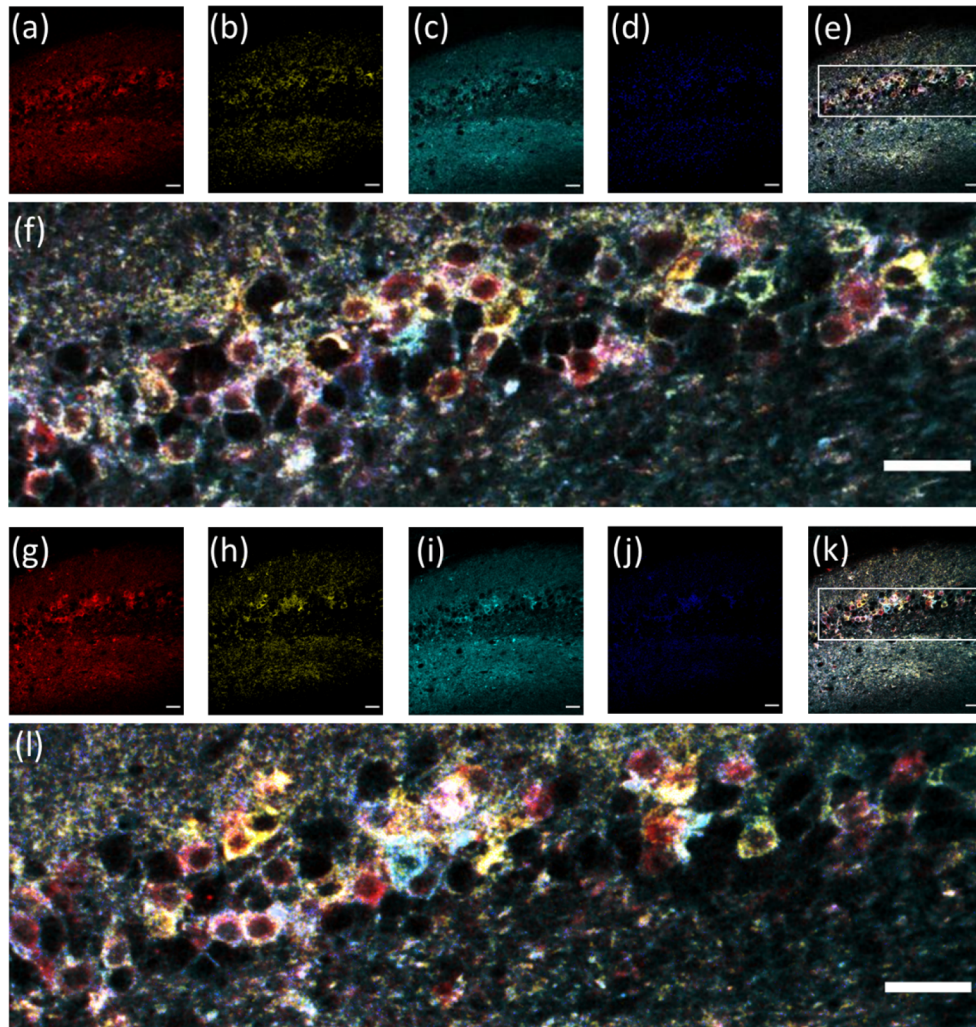


Fig. 12. Unmixed two-photon fluorescence images of the four-XFP Brainbow AAV labeled cortex of the mice brain slice at a depth of (a)–(f) 20 μm and (g)–(l) 34 μm . Unmixed single-color images expressing mCherry, EYFP, mTFP, and TagBFP are shown in (a)/(g), (b)/(h), (c)/(i), and (d)/(j), respectively. (e) and (k) shows the four-color-mixed images with (f) and (l) showing the enlarged images of the white-box areas. The image size of (a)–(e) and (g)–(k) is $5,131 \times 5,500$ pixels. The image size of the enlarged areas in (f) and (l) is $4,680 \times 1,464$ pixels. Scale bar: 50 μm .

4. Discussion

4.1. Wavelength conversion efficiency in an optical fiber

In this work, we managed to acquire a blue-shifted and dual-spectral-peaked ultrashort pulse through efficient SPM (28.5%). Other blue-shifting approaches in fibers include CR generation, doubling the frequency from red-shifted SSFS, or SPM operated in the normal dispersion region. Frequency doubling from the SSFS pulse using a nonlinear crystal is a two-stage conversion process. Thus, this approach exhibits a lower wavelength conversion efficiency (<15%) and is only recommended with a powerful source [16,35,36]. CR has been widely studied and adopted because of its high conversion efficiency (up to 65%) when the phase-matching condition is satisfied [37,38]. However, CR generation often exhibits a trade-off between wavelength conversion efficiency and blue-shifted spectral bandwidth [39]. For example, most demonstrated cases of highly efficient CR generation (>25%) have featured a narrow bandwidth (≤ 75 nm) with a single spectral peak [17,40–45], which is not suitable for providing three excitation wavelengths in one pulse. At the same time, a few reports with broad spectral coverage (full width at half-maximum (FWHM) > 100 nm) that could potentially achieve virtual wavelength generation through single-pulse compression exhibited low conversion efficiencies (<10%) [46]. SPM operated in the normal dispersion region of a fiber has been studied and implemented because it provides energy scalability without introducing complex soliton dynamics [47–49]. Typically, aside from those fully using the broadened spectrum [50,51], the wavelength conversion efficiency of the blue-shift spectrum lies between 7% and 15%, depending on the filtered spectral range [26,52–54].

Nonetheless, SPM-dominated spectral broadening operated in an anomalous dispersion region, as implemented in this work, has been reported to provide a higher wavelength conversion efficiency than that in the normal dispersion region [21]. Additionally, it is noted that when the applied fiber length (L_{fiber}) is longer than the soliton fission length (L_{fiss}), the temporal fission of a soliton might lead to more piecemeal spectral lobes and therefore reduce the spectral energy density. Thus, one is expected to acquire an improved wavelength conversion efficiency when using a fiber with its length shorter than L_{fiss} . We can estimate L_{fiss} based on the following [55]:

$$L_{\text{fiss}} \sim t_0(|\beta_2|\gamma P_p)^{-0.5}, \quad (1)$$

where β_2 is the group velocity dispersion (GVD) and t_0 is the pump pulse duration estimated from the FWHM pulse width $t_{\text{FWHM}}(t_0 \approx t_{\text{FWHM}}/1.665$ for a Gaussian pulse); $\gamma = \omega_0 n_2 / (c A_{\text{eff}})$ is the nonlinear coefficient calculated from the nonlinear refractive index n_2 and effective mode area A_{eff} of the fiber at central angular frequency ω_0 [56] with c representing the speed of light, and P_p is the input peak power. In this work, we acquired a 28.5% wavelength conversion efficiency by cleaving the HNPCF ($L_{\text{fiber}} = 6.5$ mm) shorter than our $L_{\text{fiss}} = 7.3$ mm. The short L_{fiss} is resulted from a high input peak power and an ultrashort t_0 due to the requirement of a dual-peaked spectrum generated from a sufficient nonlinear phase change. As summarized in Table 1, a previous report achieved 14% wavelength conversion efficiency by applying a 9.0-cm-long fiber, longer than its $L_{\text{fiss}} = 7.1$ cm [57], whereas another report achieved an improved wavelength conversion efficiency of 31% by applying a 8.0-cm-long fiber, which is much shorter than its $L_{\text{fiss}} = 47.3$ cm. Noted that the higher wavelength conversion efficiency in Ref. [58] might also be attributed to its lower energy shift (ΔE) compared with ours.

4.2. Other approaches for simultaneous excitation of four or more colors

In this work, we proposed and demonstrated a simple and efficient four-wavelength excitation approach to provide simultaneous excitation of four spectrally distinct FPs spanning the full visible range. Table 1 shows a comparison between the approach used here and previous three-excitation-wavelength approaches, including the multi-laser-based and the fiber-based ones,

Table 1. Comparison of wavelength conversion efficiency when operated in the anomalous dispersion region.^a

	Efficiency	L_{fiber} (mm)	L_{fiss} (mm)	ΔE (eV/photon)
Our work	28.5%	6.5	7.3	0.37
Ref. [57]	14% ^a	90	71 ^a	0.19 ^a
Ref. [58]	31% ^a	80	473 ^a	0.17 ^a

^aWavelength conversion efficiencies of Ref. [57] and [58] were calculated based on their provided average power or pulse energy. Soliton fission lengths of Ref. [57] and [58] were calculated based on their provided parameters of t_{FWHM} , β_2 , γ , and P_p derived from the given pulse energy. The γ of Ref. [57] and the β_2 of Ref. [58] could be found in their previous reports [21,59]. The values of ΔE were calculated from their given source wavelengths and the blue-shifted wavelengths.

for different combinations of fluorescent tags. As shown in Table 2, three excitation wavelengths work efficiently when using only three fluorophores [3], whereas limitations become observable when implementing simultaneous four-color imaging. In one previous study, a compromise was made to use 1,100 nm light to excite tdTomato and mCherry, with their TPA peaks being at 1,050 and 1,080 nm, respectively [15]. Lower excitation efficiency in five- and six-color applications thus became unavoidable, for example, some fluorophores were excited with over 50 nm mismatching from optimal excitation [18]. By contrast, the greater number of excitation wavelengths provided in the present work allows for efficient excitation within 15 nm mismatch from the optimal TPA wavelength and with improved excitation efficiency due to the ultrashort excitation pulse width. With the increased number of excitation wavelengths, the demonstrated fiber-format excitation source can be further applied to additional fluorophores. For future work, it is also possible to include the red-shifted part of the fiber output to provide more excitation wavelengths in the wavelength range longer than 1,100 nm.

Table 2. Comparison with three-wavelength approaches for excitation wavelength matching.

Approach	# of Ex. λ	Ex. λ (nm)	Fluorophores	TPA peaks of fluorophores (nm)	Ref.
Our work	4	812, 886, 960, 1,070	TagBFP, mTFP, EYFP, mCherry	810, 870, 970, 1,080	
Fiber-based wavelength conversion	3	864, 950, 775	TagCFP, TagYFP, TagRFP	864, 950, 775	[16]
Wavelength-mixing		750, 1,030, 1,230	DAPI, AF488, AF594	720, 950, 1,180	[17]
		850, 959, 1,100	mTurquoise2, mEYFP, tdTomato	860, 950, 1,050	[3]
			CFP, mEYFP, tdTomato, mCherry	860, 950, 1,050, 1,080	[15]
		850, 1,005, 1,230	CFP, eGFP, mOrange2, mKate2, eqFP670	860, 930, 950, 1,115, 1,110	[18,20]
	Hoechst, eGFP, K-Orange, CMTPX Red, AF647, Atto 680	800, 930, 1,120, 1,080, 1,210, 1,260			

5. Conclusion

In summary, we developed a single-laser-based, four-wavelength excitation source for simultaneously and efficiently multi-color TPFM imaging. Driven by a sub-100 fs Yb: fiber laser at 1,070 nm, we created a fiber-output spectrum dual-peaked at 812 and 960 nm with a 28.5% blue-shifting efficiency through SPM in a HNPCF in the weak negative dispersion region, with a fiber length shorter than the soliton fission length. By compressing the dual-spectral-peaked pulse to 33 fs in the focus of the TPFM, we overlapped the two peaks temporally to generate a third virtual two-photon excitation wavelength at 886 nm through SFG. Consequently, four excitation wavelengths provided by the combined TW pulse and the Yb: fiber laser pulse enabled simultaneous and efficient four-color excitation in Brainbow AAV-labeled brain samples for the first time in two-photon fluorescence microscopy. The reported fiber-format four-wavelength excitation source with the strategy of using fiber-enabled SPM combining with the SFG virtual wavelength effect represents a versatile tool providing efficient and compact multi-wavelength excitation for multicolor multi-contrast femtosecond imaging applications in biomedical research, with a cost-effective design.

Funding. Ministry of Science and Technology, Taiwan (MOST 107-2221-E-002-157-MY3, MOST 109-2321-B-002-028, MOST 110-2321-B-002-011).

Acknowledgement. We thank Prof. Ming-Chang Chen from National Tsing-Hua University, Anna Poulson from NKT photonics, and Yang Yu in Prof. Guo-Qing Chang's group from the Chinese Academy of Science for providing advice on photonic crystal fiber. We thank Prof. Shih-Hsuan Chia and Prof. Ming-Che Chan from National Yang-Ming-Chiao-Tung University for scientific discussion. We thank Prof. Chen-Tung Yen from National Taiwan University for offering suggestions on sample preparation.

Disclosures. The reported device is under a patent application process, filed dated 11th December 2020 (unpublished); U.S.A. (application no.: 17118644); inventors: C. K. Sun & Y. T. Hsiao; invention entitled, "A device for improving laser wavelength conversion efficiency and high-power multiwavelength fiber-format femtosecond laser system using the device".

Data availability. Data used in Fig. 3(b) are publicly accessible on the corresponding product website; data presented in Fig. 6 are publicly obtainable in the cited reference. The remaining data are already presented in this paper and can be obtained from the corresponding author upon reasonable request.

References

1. J. Livet, T. A. Weissman, H. Kang, R. W. Draft, J. Lu, R. A. Bennis, J. R. Sanes, and J. W. Lichtman, "Transgenic strategies for combinatorial expression of fluorescent proteins in the nervous system," *Nature* **450**(7166), 56–62 (2007).
2. D. Cai, K. B. Cohen, T. Luo, J. W. Lichtman, and J. R. Sanes, "Improved tools for the Brainbow toolbox," *Nat. Methods* **10**(6), 540–547 (2013).
3. L. Abdeladim, K. S. Matho, S. Clavreul, P. Mahou, J.-M. Sintes, X. Solinas, I. Arganda-Carreras, S. G. Turney, J. W. Lichtman, and A. Chessel, "Multicolor multiscale brain imaging with chromatic multiphoton serial microscopy," *Nat. Commun.* **10**(1), 1–14 (2019).
4. M. Inoue, A. Takeuchi, S. Manita, S.-i. Horigane, M. Sakamoto, R. Kawakami, K. Yamaguchi, K. Otomo, H. Yokoyama, and R. Kim, "Rational engineering of XCaMPs, a multicolor GECI suite for in vivo imaging of complex brain circuit dynamics," *Cell* **177**(5), 1346–1360.e24 (2019).
5. C. Ricard and F. C. Debarbieux, "Six-color intravital two-photon imaging of brain tumors and their dynamic microenvironment," *Front. Cell. Neurosci.* **8**, 57 (2014).
6. D. Maric, J. Jahanipour, X. R. Li, A. Singh, A. Mobiny, H. Van Nguyen, A. Sedlock, K. Grama, and B. Roysam, "Whole-brain tissue mapping toolkit using large-scale highly multiplexed immunofluorescence imaging and deep neural networks," *Nat. Commun.* **12**(1), 1550–1612 (2021).
7. M. Göppert-Mayer, "Über elementarakte mit zwei quantensprüngen," *Ann. Phys.* **401**(3), 273–294 (1931).
8. W. Denk, J. H. Strickler, and W. W. Webb, "Two-photon laser scanning fluorescence microscopy," *Science* **248**(4951), 73–76 (1990).
9. P. T. C. So, C. Y. Dong, B. R. Masters, and K. M. Berland, "Two-photon excitation fluorescence microscopy," *Annu. Rev. Biomed. Eng.* **2**(1), 399–429 (2000).
10. J. Pawley, *Handbook of Biological Confocal Microscopy* (Springer Science & Business Media, 2006).
11. F. Helmchen and W. Denk, "Deep tissue two-photon microscopy," *Nat. Methods* **2**(12), 932–940 (2005).
12. G. H. Patterson and D. W. Piston, "Photobleaching in two-photon excitation microscopy," *Biophys. J.* **78**(4), 2159–2162 (2000).

13. A. Hopt and E. Neher, "Highly nonlinear photodamage in two-photon fluorescence microscopy," *Biophys. J.* **80**(4), 2029–2036 (2001).
14. Z. R. Lybrand, S. Goswami, J. Zhu, V. Jarzabek, N. Merlock, M. Aktar, C. Smith, L. Zhang, P. Varma, and K.-O. Cho, "A critical period of neuronal activity results in aberrant neurogenesis rewiring hippocampal circuitry in a mouse model of epilepsy," *Nat. Commun.* **12**(1), 1423–1514 (2021).
15. P. Mahou, M. Zimmerley, K. Loulier, K. S. Matho, G. Labroille, X. Morin, W. Supatto, J. Livet, D. Débarre, and E. Beaupaire, "Multicolor two-photon tissue imaging by wavelength mixing," *Nat. Methods* **9**(8), 815–818 (2012).
16. K. Wang, T.-M. Liu, J. Wu, N. G. Horton, C. P. Lin, and C. Xu, "Three-color femtosecond source for simultaneous excitation of three fluorescent proteins in two-photon fluorescence microscopy," *Biomed. Opt. Express* **3**(9), 1972–1977 (2012).
17. K.-C. Li, L. L. Huang, J.-H. Liang, and M.-C. Chan, "Simple approach to three-color two-photon microscopy by a fiber-optic wavelength convertor," *Biomed. Opt. Express* **7**(11), 4803–4815 (2016).
18. A. Rakhymzhan, R. Leben, H. Zimmermann, R. Günther, P. Mex, D. Reismann, C. Ulbricht, A. Acs, A. U. Brandt, and R. L. Lindquist, "Synergistic strategy for multicolor two-photon microscopy: application to the analysis of germinal center reactions in vivo," *Sci. Rep.* **7**(1), 7101–7216 (2017).
19. M. Drobizhev, N. S. Makarov, S. E. Tillo, T. E. Hughes, and A. Rebane, "Two-photon absorption properties of fluorescent proteins," *Nat. Methods* **8**(5), 393–399 (2011).
20. T. J. Lambert, "FPbase: a community-editable fluorescent protein database," *Nat. Methods* **16**(4), 277–278 (2019).
21. H. Y. Chung, W. Liu, Q. Cao, L. W. Song, F. X. Kartner, and G. Q. Chang, "Megawatt peak power tunable femtosecond source based on self-phase modulation enabled spectral selection," *Opt. Express* **26**(3), 3684–3695 (2018).
22. J. Mütze, V. Iyer, J. J. Macklin, J. Colonell, B. Karsh, Z. Petrášek, P. Schwill, L. L. Looger, L. D. Lavis, and T. D. Harris, "Excitation spectra and brightness optimization of two-photon excited probes," *Biophys. J.* **102**(4), 934–944 (2012).
23. C. Xu and W. W. Webb, "Measurement of two-photon excitation cross sections of molecular fluorophores with data from 690 to 1050 nm," *J. Opt. Soc. Am. B* **13**(3), 481–491 (1996).
24. B. J. Borah, H.-H. Chi, C.-T. Yen, and C.-K. Sun, "Super-speed multiphoton microscopy for mesoscopic volume imaging with ultra-dense sampling beyond Nyquist Limit," in *Three-Dimensional and Multidimensional Microscopy: Image Acquisition and Processing XXVII* (International Society for Optics and Photonics 2020), p. 1124515.
25. W. R. Zipfel, R. M. Williams, and W. W. Webb, "Nonlinear magic: multiphoton microscopy in the biosciences," *Nat. Biotechnol.* **21**(11), 1369–1377 (2003).
26. W. Liu, C. Li, Z. Zhang, F. X. Kärtner, and G. Chang, "Self-phase modulation enabled, wavelength-tunable ultrafast fiber laser sources: an energy scalable approach," *Opt. Express* **24**(14), 15328–15340 (2016).
27. R. Stolen and C. Lin, "Self-phase-modulation in silica optical fibers," *Phys. Rev. A* **17**(4), 1448–1453 (1978).
28. J. Schindelin, I. Arganda-Carreras, E. Frise, V. Kaynig, M. Longair, T. Pietzsch, S. Preibisch, C. Rueden, S. Saalfeld, and B. Schmid, "Fiji: an open-source platform for biological-image analysis," *Nat. Methods* **9**(7), 676–682 (2012).
29. J. H. Lee, J. J. Rico-Jimenez, C. Zhang, A. Alex, E. J. Chaney, R. Barkalifa, D. R. Spillman, M. Marjanovic, Z. Arp, and S. R. Hood, "Simultaneous label-free autofluorescence and multi-harmonic imaging reveals in vivo structural and metabolic changes in murine skin," *Biomed. Opt. Express* **10**(10), 5431–5444 (2019).
30. J. N. Stirman, I. T. Smith, M. W. Kudenov, and S. L. Smith, "Wide field-of-view, multi-region, two-photon imaging of neuronal activity in the mammalian brain," *Nat. Biotechnol.* **34**(8), 857–862 (2016).
31. D. Entenberg, J. Wyckoff, B. Gligorijevic, E. T. Roussos, V. V. Verkhusa, J. W. Pollard, and J. Condeelis, "Setup and use of a two-laser multiphoton microscope for multichannel intravital fluorescence imaging," *Nat. Protoc.* **6**(10), 1500–1520 (2011).
32. A. Forlì, D. Vecchia, N. Binini, F. Succol, S. Bovetti, C. Moretti, F. Nespoli, M. Mahn, C. A. Baker, and M. M. Bolton, "Two-photon bidirectional control and imaging of neuronal excitability with high spatial resolution in vivo," *Cell Rep.* **22**(11), 3087–3098 (2018).
33. T. Zimmermann, "Spectral imaging and linear unmixing in light microscopy," in *Microscopy Techniques* 95 (Springer, 2005), pp. 245–265.
34. Y. W. Wang, N. P. Reder, S. Kang, A. K. Glaser, and J. T. Liu, "Multiplexed optical imaging of tumor-directed nanoparticles: a review of imaging systems and approaches," *Nanotheranostics* **1**(4), 369–388 (2017).
35. B. Li, M. Wang, K. Charan, M.-j. Li, and C. Xu, "Investigation of the long wavelength limit of soliton self-frequency shift in a silica fiber," *Opt. Express* **26**(15), 19637–19647 (2018).
36. J.-Y. Huang, L.-Z. Guo, J.-Z. Wang, T.-C. Li, H.-J. Lee, P.-K. Chiu, L.-H. Peng, and T.-M. Liu, "Fiber-based 1150-nm femtosecond laser source for the minimally invasive harmonic generation microscopy," *J. Biomed. Opt.* **22**(03), 1 (2017).
37. N. Akhmediev and M. Karlsson, "Cherenkov radiation emitted by solitons in optical fibers," *Phys. Rev. A* **51**(3), 2602–2607 (1995).
38. X. Liu, A. S. Svane, J. Lægsgaard, H. Tu, S. A. Boppert, and D. Turchinovich, "Progress in Cherenkov femtosecond fiber lasers," *J. Phys. D: Appl. Phys.* **49**(2), 023001 (2016).
39. G. Chang, L.-J. Chen, and F. X. Kärtner, "Fiber-optic Cherenkov radiation in the few-cycle regime," *Opt. Express* **19**(7), 6635–6647 (2011).
40. G. Chang, L.-J. Chen, and F. X. Kärtner, "Highly efficient Cherenkov radiation in photonic crystal fibers for broadband visible wavelength generation," *Opt. Lett.* **35**(14), 2361–2363 (2010).

41. J. Yuan, X. Sang, C. Yu, Y. Han, G. Zhou, S. Li, and L. Hou, "Highly efficient and broadband Cherenkov radiation at the visible wavelength in the fundamental mode of photonic crystal fiber," *IEEE Photonics Technol. Lett.* **23**(12), 786–788 (2011).
42. X. B. Zhang, X. Zhu, L. Chen, F. G. Jiang, X. B. Yang, J. G. Peng, and J. Y. Li, "Enhanced violet Cherenkov radiation generation in GeO₂-doped photonic crystal fiber," *Appl. Phys. B* **111**(2), 273–277 (2013).
43. T. Cheng, D. Deng, X. Xue, L. Zhang, T. Suzuki, and Y. Ohishi, "Highly efficient tunable dispersive wave in a tellurite microstructured optical fiber," *IEEE Photonics J.* **7**(1), 1–7 (2015).
44. M.-C. Chan, C.-H. Lien, J.-Y. Lu, and B.-H. Lyu, "High power NIR fiber-optic femtosecond Cherenkov radiation and its application on nonlinear light microscopy," *Opt. Express* **22**(8), 9498–9507 (2014).
45. I. Cristiani, R. Tediosi, L. Tartara, and V. Degiorgio, "Dispersive wave generation by solitons in microstructured optical fibers," *Opt. Express* **12**(1), 124–135 (2004).
46. H.-W. Chen, Z. Haider, J. Lim, S. Xu, Z. Yang, F. X. Kärtner, and G. Chang, "3 GHz, Yb-fiber laser-based, few-cycle ultrafast source at the Ti: sapphire laser wavelength," *Opt. Lett.* **38**(22), 4927–4930 (2013).
47. A. Chong, J. Buckley, W. Renninger, and F. Wise, "All-normal-dispersion femtosecond fiber laser," *Opt. Express* **14**(21), 10095–10100 (2006).
48. A. Hartung, A. M. Heidt, and H. Bartelt, "Design of all-normal dispersion microstructured optical fibers for pulse-preserving supercontinuum generation," *Opt. Express* **19**(8), 7742–7749 (2011).
49. A. M. Heidt, J. Rothhardt, A. Hartung, H. Bartelt, E. G. Rohwer, J. Limpert, and A. Tünnermann, "High quality sub-two cycle pulses from compression of supercontinuum generated in all-normal dispersion photonic crystal fiber," *Opt. Express* **19**(15), 13873–13879 (2011).
50. X. Liang and L. Fu, "Enhanced self-phase modulation enables a 700–900 nm linear compressible continuum for multicolor two-photon microscopy," *IEEE J. Sel. Top. Quantum Electron.* **20**(2), 42–49 (2014).
51. K. Isobe, W. Watanabe, S. Matsunaga, T. Higashi, K. Fukui, and K. Itoh, "Multi-spectral two-photon excited fluorescence microscopy using supercontinuum light source," *Jpn. J. Appl. Phys.* **44**(4), L167–L169 (2005).
52. H.-Y. Chung, W. Liu, Q. Cao, F. X. Kärtner, and G. Chang, "Er-fiber laser enabled, energy scalable femtosecond source tunable from 1.3 to 1.7 μm ," *Opt. Express* **25**(14), 15760–15771 (2017).
53. S.-H. Chia, H.-Y. Chung, W. Liu, F. X. Kärtner, and G. Chang, "Deep tissue multiphoton microscopy based on advanced femtosecond fiber sources," in *2018 20th International Conference on Transparent Optical Networks (ICTON)* (IEEE 2018), pp. 1–4.
54. L.-T. Chou, D.-L. Zhong, Y.-C. Liu, J.-C. Lee, Y.-S. Chen, and S.-H. Chia, "Widely-tunable femtosecond source tunable between 770–1180 nm for two-photon fluorescence microscopy," in *Frontiers in Ultrafast Optics: Biomedical, Scientific, and Industrial Applications XX* (International Society for Optics and Photonics 2020), p. 1127015.
55. G. P. Agrawal, "Nonlinear fiber optics," in *Nonlinear Science at the Dawn of the 21st Century* (Springer, 2000), pp. 195–211.
56. J. M. Dudley, G. Genty, and S. Coen, "Supercontinuum generation in photonic crystal fiber," *Rev. Mod. Phys.* **78**(4), 1135–1184 (2006).
57. H.-Y. Chung, R. Greinert, F. X. Kärtner, and G. Chang, "Multimodal imaging platform for optical virtual skin biopsy enabled by a fiber-based two-color ultrafast laser source," *Biomed. Opt. Express* **10**(2), 514–525 (2019).
58. P. Wang, X. Xu, Z. Guo, X. Jin, and G. Shi, "926 nm Yb-doped fiber femtosecond laser system for two-photon microscopy," *Appl. Phys. Express* **12**(3), 032008 (2019).
59. Z. Guo, Q. Hao, K. Yang, and H. Zeng, "A two-stage optical parametric amplifier for femtosecond fiber laser generation at 920 nm," *Opt. Commun.* **425**, 166–171 (2018).